Ultrasonics - Sonochemistry 43 (2018) 166–174

Contents lists available at ScienceDirect

Ultrasonics - Sonochemistry

journal homepage: www.elsevier.com/locate/ultson

Dynamic behaviour of a two-microbubble system under ultrasonic wave excitation

Xiao Huang[a,d], Qian-Xi Wang[b,c], A-Man Zhang[a], Jian Su[d,*]

[a] College of Shipbuilding Engineering, Harbin Engineering University, Harbin 150001, PR China
[b] School of Mathematics, The University of Birmingham, Ring Rd N, Birmingham B15 2TS, United Kingdom
[c] School of Naval Architecture, Dalian University of Technology, Dalian 116024, PR China
[d] Nuclear Engineering Program, COPPE, Universidade Federal do Rio de Janeiro, CP 68509, Rio de Janeiro 21941-972, Brazil

ARTICLE INFO

Keywords:
Microbubble dynamics
Ultrasonic wave
Boundary element method

ABSTRACT

Acoustic bubbles have wide and important applications in ultrasonic cleaning, sonochemistry and medical ultrasonics. A two-microbubble system (TMS) under ultrasonic wave excitation is explored in the present study, by using the boundary element method (BEM) based on the potential flow theory. A parametric study of the behaviour of a TMS has been carried out in terms of the amplitude and direction of ultrasound as well as the sizes and separation distance of the two bubbles. Three regimes of the dynamic behaviour of the TMS have been identified in terms of the pressure amplitude of the ultrasonic wave. When subject to a strong wave with the pressure amplitude of 1 atm or larger, the two microbubbles become non-spherical during the first cycle of oscillation, with two counter liquid jets formed. When subject to a weak wave with the pressure amplitude of less than 0.5 atm, two microbubbles may be attracted, repelled, or translate along the wave direction with periodic stable separation distance, depending on their size ratio. However, for the TMS under moderate waves, bubbles undergo both non-spherical oscillation and translation as well as liquid jet rebounding.

1. Introduction

Cavitation bubbles are associated with the erosion and noise of hydraulic machines, propellers and turbines [1,2]. Acoustic cavitation bubbles are applied in cavitation cleaning [3,4], extracorporeal shock wave lithotripsy (ESWL) [5], drug delivery and sonoporation [6].

A two-microbubble system (TMS) is a basic unit of bubble clusters. Theoretical studies were carried out for two spherical bubbles subject to acoustic waves. Crum derived the formula for calculating the 'secondary Bjerknes force' for the interaction of two oscillating spherical bubbles subject to an acoustic wave [7]. This model was later developed by considering the viscous and thermal effects [8,9], bubbles at different sizes [10] and under dual-frequency ultrasound [11], as well as in viscoelastic fluid [12]. Microstreaming generated by two acoustically induced spherical bubbles was studied by Doinikov and Bouakaz [13]. The interaction of two approximate spherical encapsulated bubbles was studied by using perturbation theory based on the potential flow theory by Liu and Wang [14].

The interaction of non-spherical transient bubbles was modelled by numerical methods. The domain methods coupled with the interface capturing techniques present good results for computing the collapse, coalescence, and splitting of three-dimensional (3-D) bubbles [15–17]. The interaction of two bubbles was modelled by Han et al. by using the boundary element method (BEM) [18,19]. Multiple bubbles dynamics was simulated by using the BEM coupled with fast multiple expansions [20–22]. Multibubble surface cavitation can be achieved by using a strong negative impulsive liquid pressure wave to expand the nuclei in the microcavities. Interaction of two or more pulsating microbubbles formed in this way was investigated both experimentally and numerically by Bremond et al. [23,24]. Jet formation during the evolution of two microbubbles near a solid wall has been observed [23].

In this paper we consider the interaction of two initially spherical microbubbles subject to ultrasound with different pressure amplitude, which may become non-spherical due to close interactions and/or strong ultrasonic wave (Wang and Manmi [25,26]; Ochiai and Ishimoto [4]). The dynamics of a single non-spherical bubble subject to ultrasound was simulated by using the BEM (Klaseboer et al. [27]; Calvisi et al. [28,29]; Wang and Blake [30,31]; Wang and Manmi [25,26]). The physical and numerical models are introduced in Section 2. In Section 3, the numerical model is firstly validated against an axisymmetric model, and a parametric study of the behaviour of a TMS is then carried out in terms of the amplitude and direction of ultrasound, the sizes, and

* Corresponding author.
E-mail address: sujian@nunclear.ufrj.br (J. Su).

https://doi.org/10.1016/j.ultsonch.2018.01.012
Received 10 November 2017; Received in revised form 9 January 2018; Accepted 9 January 2018
Available online 10 January 2018
1350-4177/

separation distance of the two bubbles. Finally, concluding remarks are given in Section 4.

2. Boundary element method

Consider a two-microbubble system (TMS) subject to an ultrasonic wave, as illustrated in Fig. 1. The two bubbles are labeled as bubble 1 and bubble 2 with the initial radii R_{01} and R_{02} respectively. The initial separation distance between their centres C_1 and C_2 is denoted as D. A Cartesian coordinate system is set with its origin O at the midpoint of the initial centreline C_1C_2 and the x-axis is in the direction of wave propagation. The centreline C_1C_2 lies in the Oxz plane, with an angle β with the x-axis.

The far-field pressure p_∞ is given by

$$p_\infty(x,t) = p_0 + p_a \sin(kx - 2\pi ft), \tag{1}$$

where p_0 is the hydrostatic pressure, p_a the pressure amplitude of the wave, k the wave number, and f the wave frequency.

We assume that the flow is incompressible and potential, the velocity potential φ thus satisfies Laplace's equation

$$\nabla^2\varphi = 0. \tag{2}$$

Assuming that each bubble undergoes adiabatic process during the motion [26], the internal gas pressure p_{bi} of bubble i is given by

$$p_{bi} = p_v + p_{gi0}\left(\frac{V_{0i}}{V_i}\right)^\alpha, \tag{3}$$

where p_v is the saturated vapor pressure, p_{gi0} the initial partial pressure of a non-condensible gas in bubble i, V_{0i} and V_i are its initial and transient volumes, respectively, α is the polytropic index of the bubble gas, which is set as 1.4 in this work.

The liquid pressure p on bubble surface S_{bi} satisfies the Young–Laplace equation

$$p = p_{bi} - 2\sigma\kappa \quad \text{on } S_{bi}, \tag{4}$$

where σ is surface tension and κ the local curvature of the bubble surface.

The Bernoulli equation for incompressible potential flows reads

$$\rho\frac{\partial\varphi}{\partial t} + \frac{\rho}{2}|\nabla\varphi|^2 + p - p_\infty = 0, \tag{5}$$

where ρ is the liquid density. Substituting Eqs. (1), (3) and (4) into (5) yields the dynamic boundary condition on bubble surfaces

$$\rho\frac{\partial\varphi}{\partial t} + \frac{\rho}{2}|\nabla\varphi|^2 + p_v + p_{gi0}\left(\frac{V_{0i}}{V_i}\right)^\alpha - 2\sigma\kappa - p_0 - p_a\sin(kx - 2\pi ft) = 0. \tag{6}$$

Using matched asymptotic expansions, Wang and Blake [30,31] showed that the flow far away from the bubble can be described by the linear wave equation to second order in terms of the Mach number while the flow near the bubble can be described by Laplace's equation

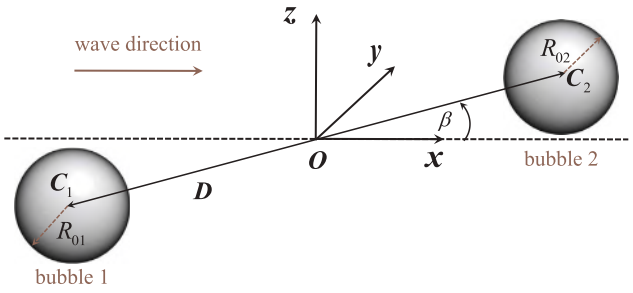

Fig. 1. Sketch of a TMS subject to a travelling ultrasonic wave and the coordinate system.

to second order. This weakly compressible theory shows that the incident wave effects can be approximated to second order as the last term of the boundary condition (6).

To perform non-dimensionalization, the length scale is chosen as the initial radius R_{01} of bubble 1, the pressure scale $\Delta p = p_0 - p_v$, and the reference velocity $U = \sqrt{\Delta p/\rho}$. The corresponding reference time is $T = R_{01}/U$. The dimensionless parameters and variables are labeled by the superscript '*', as follows

$$D^* = \frac{D}{R_{01}},\ t^* = \frac{t}{T},\ f^* = fT, \tag{7a}$$

$$\varphi^* = \frac{\varphi}{UR_{01}},\ \sigma^* = \frac{\sigma}{R_{01}\Delta p},\ k^* = kR_{01}. \tag{7b}$$

The dimensionless dynamic boundary condition (6) becomes

$$\frac{d\varphi^*}{dt^*} = 1 - p^*_{gi0}\left(\frac{V^*_{0i}}{V^*_i}\right)^\alpha + \frac{1}{2}|\nabla\varphi^*|^2 + 2\sigma^*\kappa^* + p^*_a\sin(k^*x^* - 2\pi f^*t^*). \tag{8}$$

Note that the partial derivative in Eq. (6) is converted to the material derivative using the relation $d\varphi^*/dt^* \equiv \partial\varphi^*/\partial t^* + \boldsymbol{v}^*\cdot\nabla\varphi^*$, where $\boldsymbol{v}^*$ is the velocity. The kinematic boundary condition is essential for tracking the position $\boldsymbol{r}^*$ of each particle on bubble surfaces:

$$\frac{d\boldsymbol{r}^*}{dt^*} = \boldsymbol{v}^*. \tag{9}$$

The velocity potential φ^* satisfies the following boundary integral equation (BIE)

$$c(\boldsymbol{r}^*)\varphi^*(\boldsymbol{r}^*) = \int\int_S \left[\frac{\partial\varphi^*(\boldsymbol{q}^*)}{\partial n}G(\boldsymbol{r}^*,\boldsymbol{q}^*) - \varphi^*(\boldsymbol{q}^*)\frac{\partial G(\boldsymbol{r}^*,\boldsymbol{q}^*)}{\partial n}\right]dS, \tag{10}$$

where S denotes all surfaces of bubbles; $c(\boldsymbol{r}^*)$ is solid angle, $\boldsymbol{r}^*$ and $\boldsymbol{q}^*$ are the field and source points, respectively and $\boldsymbol{n}$ is the unit outward normal vector of bubble surfaces. The Green function is $G(\boldsymbol{r}^*,\boldsymbol{q}^*) = |\boldsymbol{q}^* - \boldsymbol{r}^*|^{-1}$.

The surfaces of the initially spherical bubbles are meshed into triangles based on regular icosahedrons [32]. The bubbles are at rest at the beginning of simulation. Hence, both the velocity potential φ^* and the velocity $\boldsymbol{v}^*$ of each node on bubble surfaces equal zero at $t^* = 0$. The normal velocity $\partial\varphi^*/\partial n$ of each node is calculated using Eq. (10) in every time step. The tangential velocity is calculated using the interpolation of the bubble surface and the velocity potential on the surface [33].

φ^* and $\boldsymbol{r}^*$ are then updated by integrating the dynamic and kinematic boundary conditions (8) and (9), respectively. An explicit fourth-order Runge–Kutta (RK4) scheme is used in the numerical integration. A weighted least-squares smoother [19] is used every 30 time steps to keep the bubble surfaces smooth.

A time step $\Delta t^* = \min(\Delta t^*_{\boldsymbol{v}}, \Delta t^*_\varphi)$ is used, with

$$\Delta t^*_{\boldsymbol{v}} = \frac{\min(l^*_{edge})}{\max(|\boldsymbol{v}^*|)},\quad \Delta t^*_\varphi = \frac{\varphi^*_{cr}}{\max(d\varphi^*/dt^*)}, \tag{11}$$

where l^*_{edge} denotes the length of bubble element edge, φ^*_{cr} is a constant used to restrict the increment of the velocity potential, and the maximum and minimum in (11) are taken for all nodes on bubble surfaces. In this paper, we set $\varphi^*_{cr} = 0.01$, unless specified otherwise.

The field pressure p^*_f is given by the Bernoulli equation

$$p^*_f = 1 + p^*_v + p^*_a\sin(k^*x^* - 2\pi f^*t^*) - \frac{\partial\varphi^*}{\partial t^*} - \frac{1}{2}|\nabla\varphi^*|^2. \tag{12}$$

It is a well-known challenge to calculate the pressure field associated with bubble dynamics. Calculating the term $\partial\varphi^*/\partial t^*$ in (12) using a finite difference method often results in unacceptable errors, due to very small time steps usually used for simulating a violent collapsing bubble. We calculate $\partial\varphi^*/\partial t^*$ using the BEM model since $\partial\varphi^*/\partial t^*$ satisfies Laplace's equation, too, following Tanizawa [34] and Wu [35]. We also calculate $\nabla\varphi^*$ using the BEM since $\partial\varphi^*/\partial x^*$, $\partial\varphi^*/\partial y^*$ and $\partial\varphi^*/\partial z^*$ satisfy

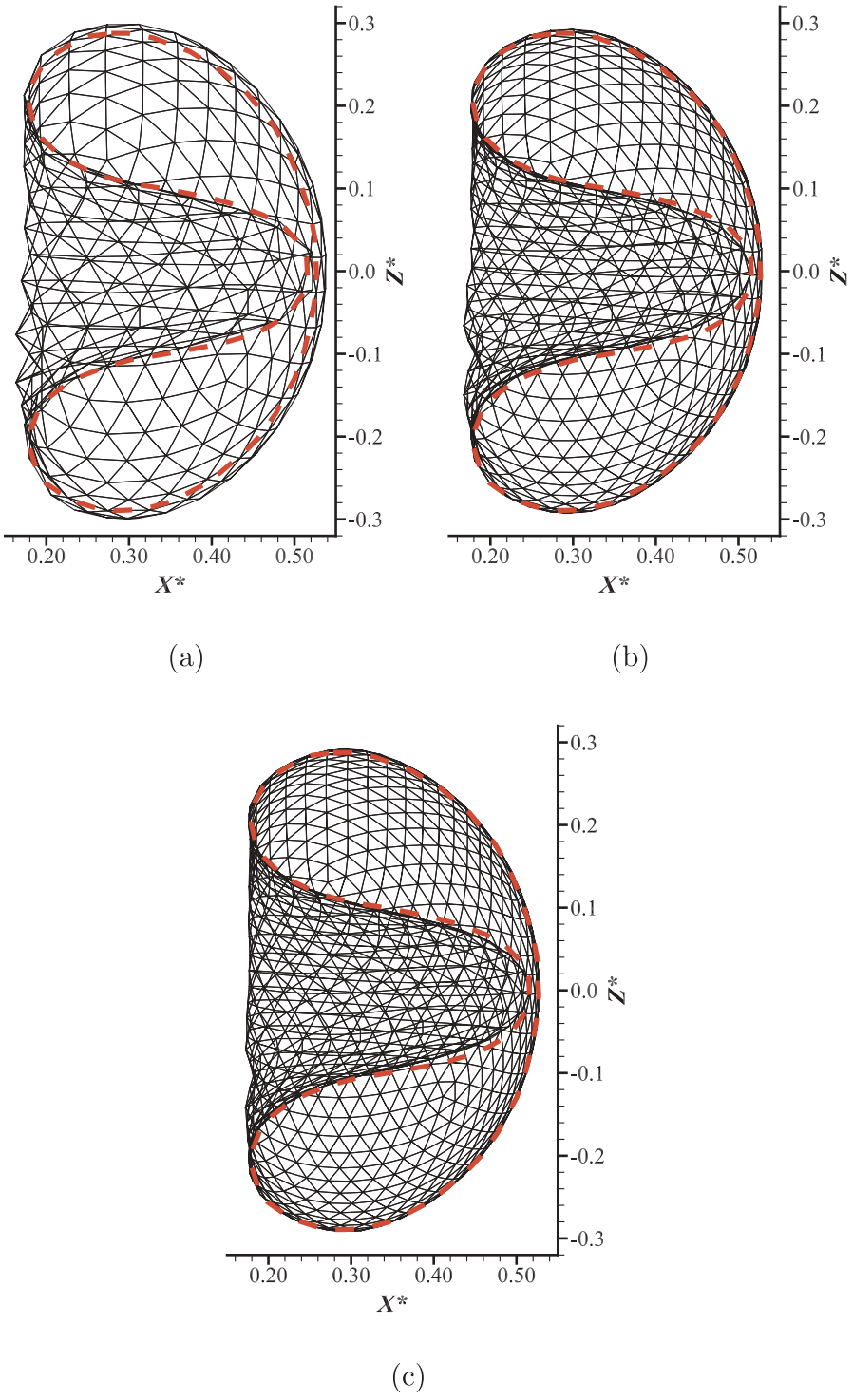

Fig. 2. Comparison of bubble shapes at the end of the collapse phase ($t^* = 5.637$) with an axisymmetric BEM (dashed line, Calvisi et al. [28]). (a) 720 elements, (b) 980 elements, and (c) 1280 elements. $p_a^* = 1.6$, $R_0 = 4.5\,\mu m$, $f^* = 0.136$ (in dimensional, 0.3 MHz), $\alpha = 1.667$ and $\rho = 998\,kg\,m^{-3}$.

Laplace's equation as well.

3. Numerical analysis

In the following calculations, the surface tension is taken as $\sigma = 0.073 N\,m^{-1}$, the liquid density $\rho = 998\,kg\,m^{-3}$, the hydrostatic pressure $p_0 = 101.3\,kPa$ and the saturated vapor pressure $p_v = 2339\,Pa$.

3.1. Comparison with axisymmetric BEM

The case is for a single bubble with an initial radius $R_0 = 4.5\,\mu m$, subject to a travelling ultrasound with a pressure amplitude $p_a^* = 1.6$ and a frequency $f^* = 0.136$ (in dimensional, 0.3 MHz). The polytropic index of the bubble gas is $\alpha = 1.667$. Fig. 2 compares the bubble shapes calculated from the present 3-D model and the axisymmetric model [28]. Agreement between the two models improves as the mesh density increases.

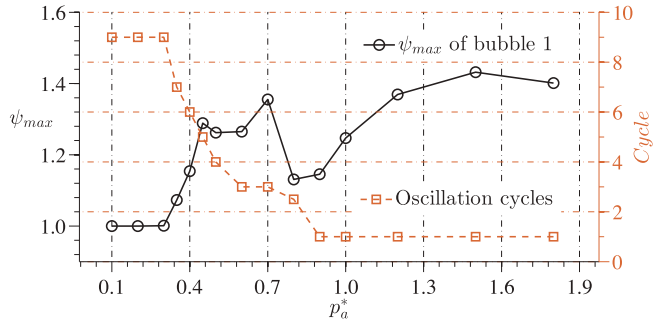

Fig. 3. Oscillation cycles of a TMS and the maximum sphericity $\psi_{\max}$ of bubble 1 at different ultrasonic wave pressure amplitude p_a^*. $\beta = 0$, $R_{01}^* = R_{02}^* = 1$ (in dimensional, 5 μm), $f^* = 0.151$ (0.3 MHz) and $D^* = 6$.

3.2. General features

Bubbles may become non-spherical when subject to acoustic waves. We use the sphericity ψ to describe the deviation extent of a bubble from a spherical shape [36]:

$$\psi = \frac{A_b}{\pi^{1/3}(6V_b)^{2/3}}, \tag{13}$$

where A_b and V_b denote the surface area and the volume of a bubble, respectively. Notice $\psi = 1$ for a sphere and $\psi > 1$ for all the non-spherical geometries.

Fig. 3 shows the overall dynamic behaviour of the TMS under ultrasonic wave forcing in terms of the maximum sphericity of bubble 1 and the number of cycles that the TMS has oscillated (the average volume oscillation cycles of the two bubbles) before the termination of simulation. The simulation is either terminated at $t^* = 30$ or at the moment when any liquid jet impacts on the opposite side of the bubble surface. It can be seen from Fig. 3 that the bubble dynamic behaviour can be divided into three categories: high pressure amplitude ($p_a^* > 1.0$), moderate pressure amplitude ($0.5 \leqslant p_a^* \leqslant 1.0$) and low pressure amplitude ($p_a^* < 0.5$). When under strong acoustic wave ($p_a^* > 1.0$), the bubbles become significantly non-spherical associated with a larger maximum sphericity $\psi_{\max}$ and the liquid jets form in the first cycle of oscillation and impact on the opposite bubble surface. These inertial collapse behaviour is associated with applications in surface cleaning [37] and lithotripsy [38]. For a weak acoustic wave ($p_a^* < 0.5$), the bubbles stay nearly spherical for a relative long time and oscillate for many cycles without jet formation. The maximum sphericity $\psi_{\max}$ stays at the value 1 while the oscillation cycles exceed 6 as can be seen in the figure. The number of bubble oscillation cycles is 9 for p_a^*=0.1–0.3 up to dimensionless time $t^* = 30$ (equivalent roughly to 4.53 acoustic cycles), as the dimensionless natural frequency of the bubble, being 0.32, is about two times of the driving wave frequency 0.151. On this occasion, their translational motion and oscillation are worth studying. This kind of stable repeated oscillation of bubbles are associated with sonography [38] and sonochemistry [39]. The cases

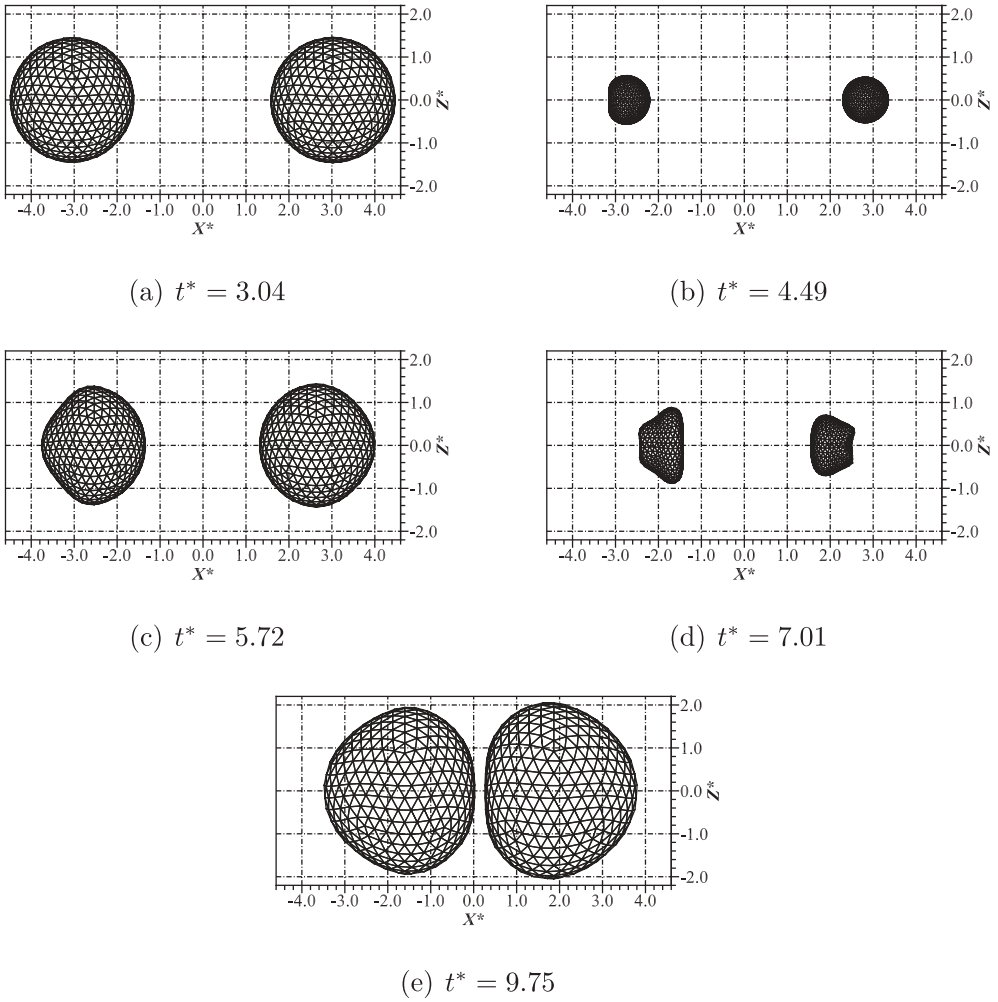

Fig. 4. TMS under moderate wave forcing when bubble 1 reaches its first, second and third maximum volumes (frames (a), (c) and (e)) and its first and second minimum volumes (frames (b) and (d)). $p_a^* = 0.8$, $\beta = 0$, $R_{01}^* = R_{02}^* = 1$ (in dimensional, 5 μm), $f^* = 0.151$ (0.3 MHz) and $D^* = 6$.

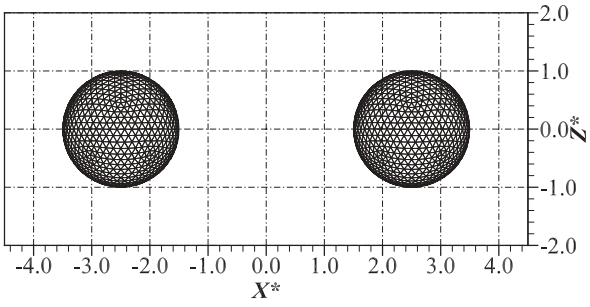

(a) $t^* = 0$

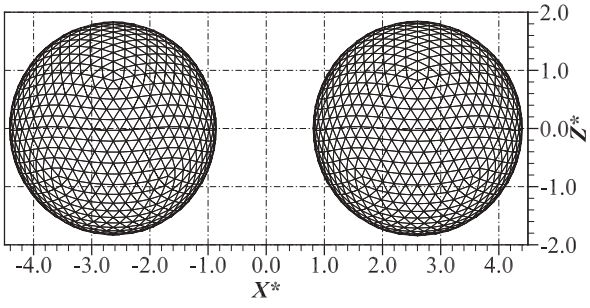

(b) $t^* = 3.43$

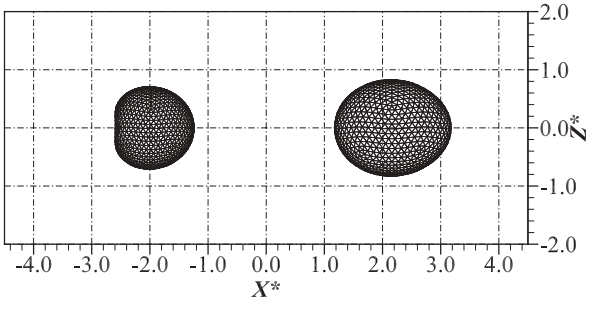

(c) $t^* = 4.84$

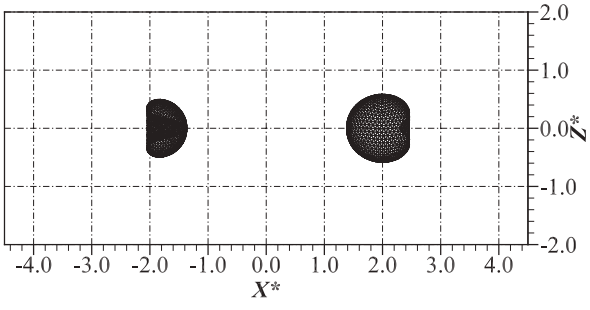

(d) $t^* = 4.90$

Fig. 5. Bubble shapes of a TMS under strong wave forcing. $p_a^* = 1.2$, $\beta = 0$, $R_{01}^* = R_{02}^* = 1$ (in dimensional, 5 μm), $f^* = 0.151$ (0.3 MHz) and $D^* = 5$.

shown in Fig. 3 are for the dimensionless initial spacing $D^* = 6$ between two bubbles. Our calculations for $D^* \in [5,20]$ with remaining parameters unchanged have shown that the TMS presents similar behaviour shown in Fig. 3 for both strong and weak wave amplitude regions.

As a TMS is subject to moderate acoustic wave forcing, the behaviour of a TMS in both strong and weak wave regions may be observed. Fig. 4 shows a case for $p_a^* = 0.8$. The acoustic wave induces a liquid jet with bubble 1 at the end of the first cycle (Fig. 4(b)). However, the wave is not strong enough to cause a jet penetration through the opposite side of the bubble, like in Fig. 2 for a strong wave. Instead, the bubble start rebounding during jet development and the jet disappears before it reaches maximum volume (Fig. 4(c)). The liquid jet re-appears at the end of bubble re-collapse (Fig. 4(d)). Likewise, this time the jet is still not fast enough to penetrate the bubble; it bounces back again when the bubble starts to expand in the third cycle. When the bubble 1 reaches its maximum volume in this cycle (Fig. 4(e)), two bubbles are close to each other and are about to coalesce. In this process, bubble 2 behaves similarly to bubble 1 with a slight delay. In this category, bubbles undergo both non-spherical oscillation and translation.

3.3. Subject to strong ultrasound

Consider two bubbles having initial radii 5 μm and the initial spacing $D^* = 5$ subject to an acoustic wave with $p_a^* = 1.2$ and $f^* = 0.151$ (in dimensional, 0.3 MHz). Single acoustic bubble dynamics in this parameter family was widely studied [28,40,25,26]. The interaction of two microbubbles near the solid wall induced by a stronger negative pressure impulse was investigated by an axisymmetric BEM model [24]. In the present case, bubble 1 reaches its maximum volume at $t^* = 3.43$ (see Fig. 5(b)), and both bubbles keep spherical shapes until this moment. The bubbles become non-spherical at the end of collapse due to the acoustic wave as well as the interaction between bubbles. Dominated by the secondary Bjerknes force, the two bubbles are attracted to each other with the formation of two counter jets. While the two microbubbles investigated by Bremond et al. [23] are symmetrical to each other, the two microbubbles investigated here clearly undergo different dynamical processes. Bubble 1, located in front to the traveling wave, presented much larger volume oscillation, loss of sphericity, and jet formation than bubble 2.

Fig. 6 shows the time histories of the two jet velocities. The jets of bubble 1 and bubble 2 reach their maximum velocities at $t^* = 4.84$ and $t^* = 4.90$ respectively, during the early stage of development of the two jets, as shown in Figs. 5(c) and 5(d), respectively. After that, the jet velocities firstly drop slightly and then do not vary significantly before jet impact.

Fig. 7 shows the convergence tests for the case in Fig. 6, for the jet velocity histories in the late stage of the collapse phase of bubble 1 in terms of mesh sizes and time steps. It can be seen that a smaller mesh size and/or a shorter time step lead to the liquid jet forming slightly later with a higher speed. The results converge approximately for 980 elements and $\varphi_{cr}^* = 0.01$. These two values for the mesh size and time step are used in the following cases to ensure the accuracy and efficiency.

Fig. 8 shows the pressure field around bubble 1 at the *Oxz*-plane during jet development under strong wave forcing. At this time, each bubble is more affected by the other bubble than by the ultrasonic wave, due to the strong interaction between the bubbles. A high pressure zone is formed at the base of the jet and its amplitude increases with time as the jet develops, whilst the pressure on the other side of the bubble is relatively smaller. The pressure difference across the bubble drives the motion of the jet. During the formation of the jet, the bubble surface on the other side of the jet does not deviate significantly from the spherical form.

Fig. 9 displays the time histories of the volumes of two bubbles. One can see from Figs. 8(d) and 9 that bubble 1 reaches its minimum volume before the jet penetrates through the other side. We believe that this 'early maximum jet velocity' and 'early bubble rebound' is due to the 'not-so-strong' wave pressure amplitude p_a^*. According to our calculations, the maximum jet velocity occurs at the early stage of jet formation, for the wave pressure amplitude $p_a^* \in [1.0,1.5]$, and the initial

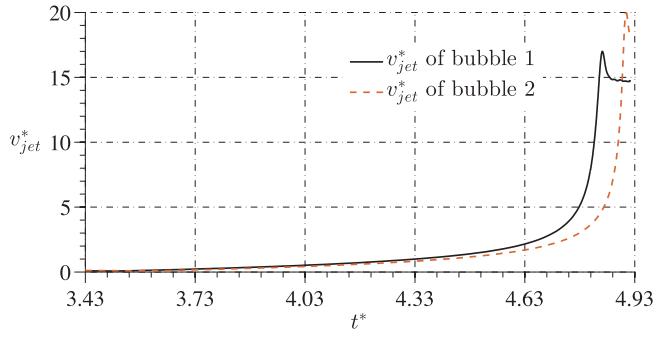

Fig. 6. Jet velocities of a TMS in the compression phase as functions of time for the case in Fig. 5.

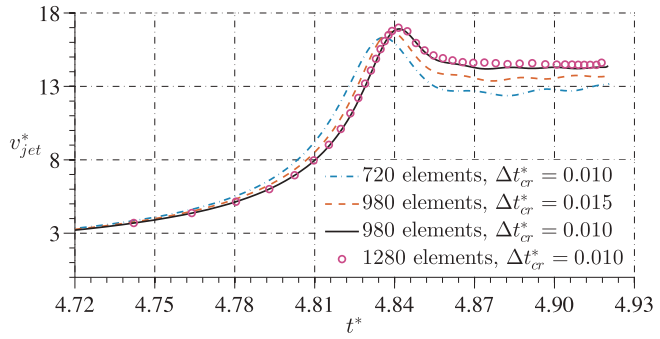

Fig. 7. Jet velocity histories during the late stage of the collapse phase of bubble 1 for the case in Fig. 6 with different mesh sizes and time steps.

spacing $D^* \in [5,20]$. The jet velocity will keep increasing until jet penetration for $p_a^* > 1.6$.

Note the jet of bubble 2 forms later than that of bubble 1 with a higher maximum velocity (Fig. 6), and has a larger maximum volume and a longer period (Fig. 9)). Fig. 9 also displays the time history of the pressure at the initial centre of the TMS, whose amplitude is one order larger than that of the wave pressure.

In the above cases, the two bubbles are placed along the wave direction, i.e. $\beta = 0$. Fig. 10 shows the maximum jet velocities and the corresponding time when maximum jet velocities occur in function of β. As β increases from 0 to $\pi/2$, the difference of the maximum dimensionless jet velocities between bubble 1 and 2 decreases from 4 (in dimensional value, 40 m s^{-1}) to 0.

3.4. Subject to weak ultrasound

When subject to weak ultrasound, i.e. $p_a^* < 0.5$, a TMS undergoes steady oscillation for many cycles. We terminate the simulation at $t^* = 30$ here, which is sufficient for studying the dynamics of the TMS.

3.4.1. Equal sized TMS

The case considered is for $p_a^* = 0.3$ and $\beta = 0$, with the remaining parameters being the same as in Fig. 4. Both bubbles are nearly spherical during the whole simulation process, as their sphericity ψ is less than 1.001. As shown in Fig. 11, each violent oscillation cycle is followed by a mild one and the bubbles oscillate approximately twice per acoustic period. The natural frequency f_n^* of a bubble is given by Wang and Blake [30]

$$f_n^* = \frac{1}{2\pi R_0^*}\sqrt{3\alpha}, \tag{14}$$

where R_0^* is the equilibrium radius of a bubble. The natural frequency of the bubbles considered being 0.32 is about two times of the driving wave frequency 0.151.

The time history of the centroid displacement C_x^* of the two bubbles is also shown in the figure. The magnitude of C_x^* denotes the displacement of a bubble from its initial position and the sign depicts the translational direction. The bubbles migrate towards the initial centre of configuration with their speeds increasing with time. The secondary Bjerknes force between the two bubbles is predominant in this case.

As $\beta \neq 0$, the bubbles translate along both the x- and z-axes. Fig. 12 displays the time histories of the average displacement of the bubble centroids

$$C_{as}^* = \frac{\int_0^{t_1} C_s^* \, dt}{t_1}, \tag{15}$$

where the subscript 's' denotes 'x' or 'z' and t_1 is the total time used in simulation. The two bubbles translate in opposite directions with approximately the same speed. The bubble translation in this case is again dominated by the secondary Bjerknes force.

3.4.2. Unequal sized TMS

In this section, translation of two bubbles with unequal initial sizes is investigated. The initial radius of bubble 1 is 5 μm while that of bubble 2 varies with a larger size. The initial spacing is set as $D^* = 20$, to examine a relative larger range of R_{02}^*. The remaining parameters are the same as in Fig. 11.

Fig. 13 presents the results of the case $R_{02}/R_{01} = 2$. Since the larger bubble dominates the behaviour of the TMS, only the volume history of bubble 2 is depicted here. The natural frequency f_n^* of bubble 2 calculated using (14) being 0.163 is close to the wave frequency 0.151. Bubble 2 undergos resonance with its oscillation amplitude increasing monotonically. Fig. 13 also displays the time history of the displacement of the bubble centroids. Both bubbles migrate along the wave direction at similar amplitude, with much smaller relative motion. The separation distance between the bubbles is periodic stable, which is consistent with the conclusion of Barbat et al. [8]. In this case, the primary Bjerknes force [41] due to the acoustic wave is predominant.

Fig. 14 shows the time history of the displacement of the bubble centroids for $R_{02}^* = 8$. The initial volume ratio of two bubbles here reaches 512. In this case, the dimensionless time scale only covers one cycle of oscillation of bubble 2. During the time period, the center of bubble 2 does not migrate significantly while bubble 1 is pushed away by bubble 2 and undergoes oscillating translation following the oscillating bubble 2.

Fig. 15 shows the time histories of the bubble centroids for bubble 1 and bubble 2 for 4 different size ratios $R_{02}^* = 1, 2, 4, 8$. The two bubbles are attracted to each other for $R_{02}^* = 1$, translate along the wave direction for $R_{02}^* = 2$, and the small bubble leaves away from the large one which does not translate significantly for $R_{02}^* = 4, 8$. These characteristics were also predicted by the linear analysis of two spherical bubbles subject to an acoustic wave [7,8].

4. Summary and conclusions

The dynamics of a two-microbubble system (TMS) subject to an ultrasonic wave is investigated by using the boundary element method (BEM) based on the potential flow theory. The numerical model is verified by comparing with an axisymmetric BEM as well as convergence test. The pressure distribution in the flow field is calculated by using the Bernoulli equation, where the partial derivative of the velocity potential in time is calculated using the BEM to avoid numerical instabilities.

Numerical analysis is performed for a two bubble system for bubbles with equilibrium radii about 5 μm and initial spacing from 25 to 100 μm subject to the wave with a frequency of $f = 0.3$ MHz and pressure amplitude from 0.5 to 2 atm. Three regimes of the dynamic behaviour of the TMS have been identified in terms of the pressure amplitude of ultrasound as following.

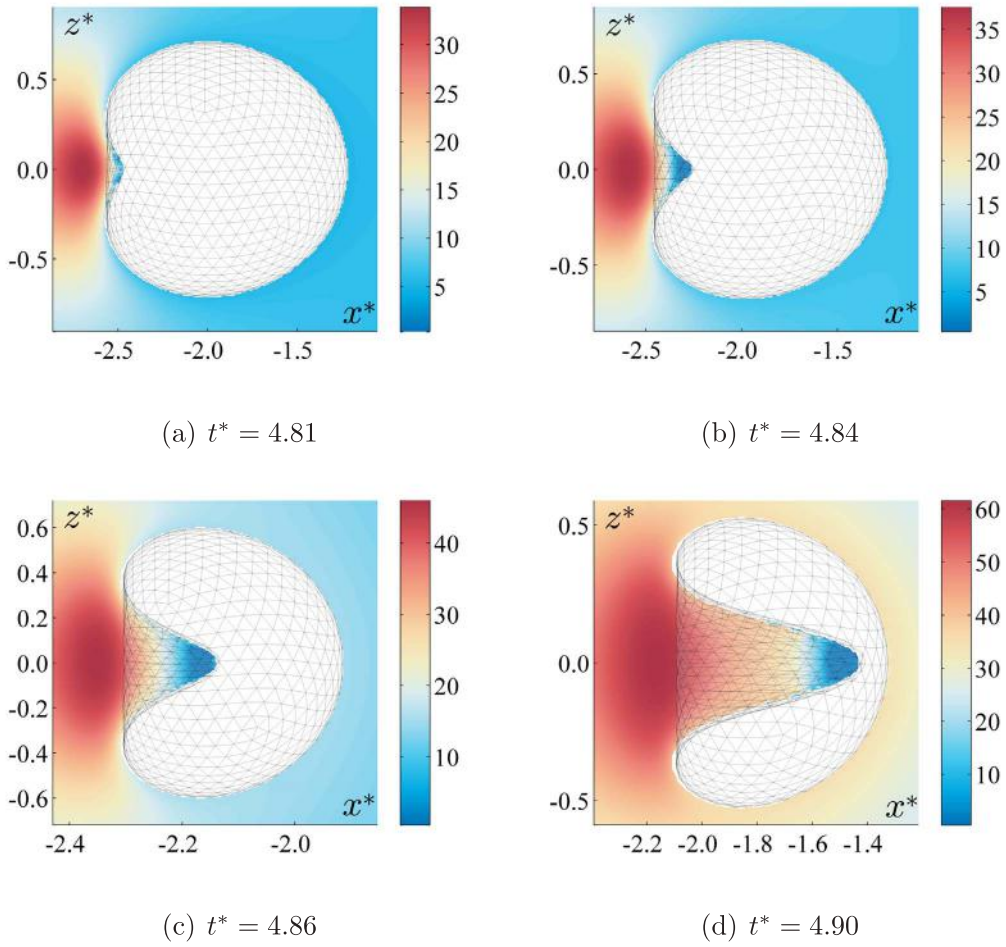

Fig. 8. Pressure field p_f^* near bubble 1 as the bubble jet develops for the case in Fig. 5.

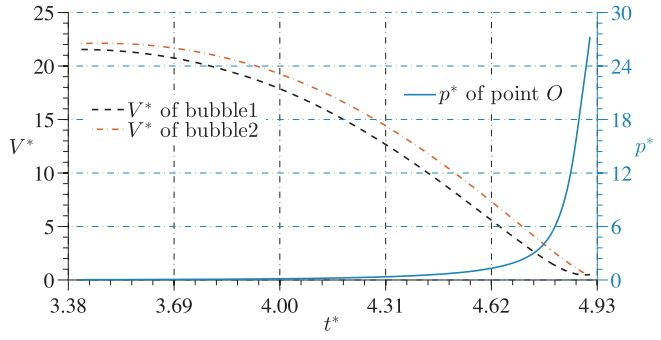

Fig. 9. Time histories of the bubble volumes and pressure at the initial centre O of the configuration for the case in Fig. 5.

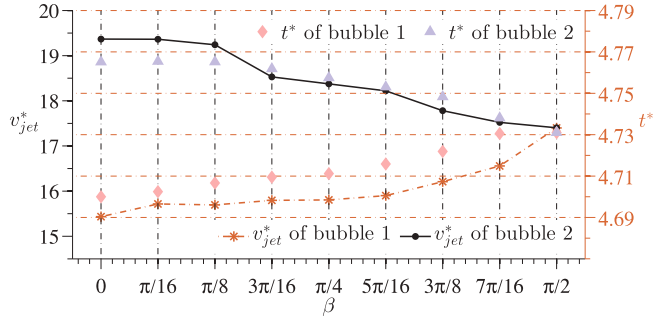

Fig. 10. The maximum jet velocity v^*_{jet} of each bubble and their corresponding occurrence time as functions of β. The remaining parameters are the same as in Fig. 5

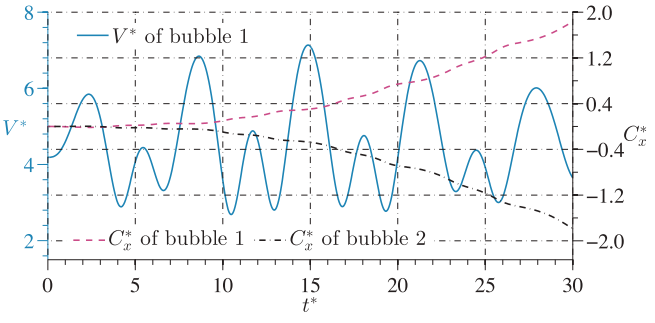

Fig. 11. Time histories of the geometric centres of the bubbles in the x direction and the volume of bubble 1 for $p_a^* = 0.3$, $\beta = 0$, $R_{01}^* = R_{02}^* = 1$, $f^* = 0.151$ and $D^* = 6$.

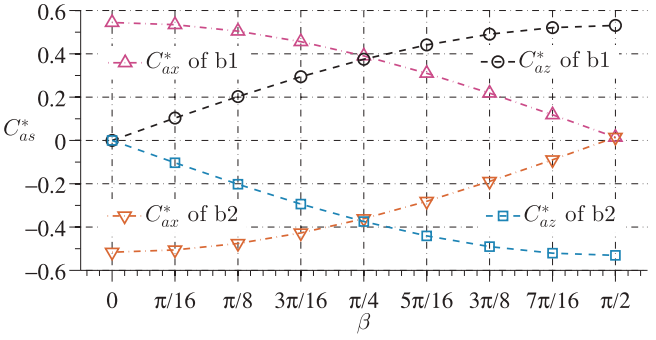

Fig. 12. Time histories of the displacement of the bubble controids C_{ax}^* and C_{az}^* in terms of β. The remaining parameters are the same as in Fig. 11.

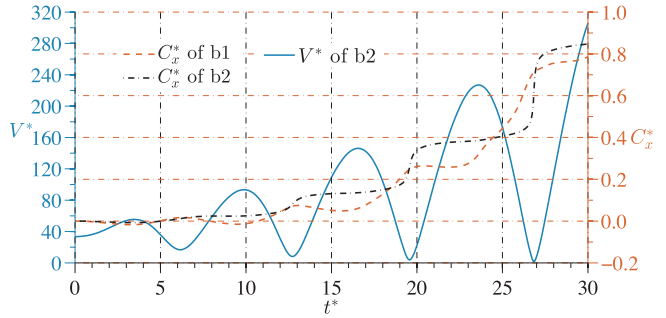

Fig. 13. Time histoires of the centroids C_x^* of the two bubbles and the volume V^* of bubble 2 for $R_{02}^* = 2$ and $D^* = 20$. The remaining parameters are the same in Fig. 11.

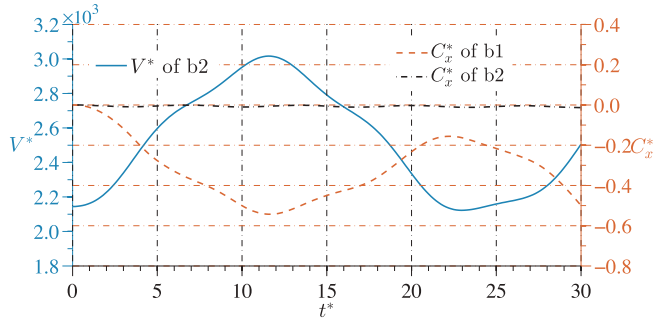

Fig. 14. Time histories of the centroids C_x^* of the two bubbles and the volume V^* of bubble 2 for $R_{02}^* = 8$ and $D^* = 20$. The remaining parameters are the same in Fig. 11.

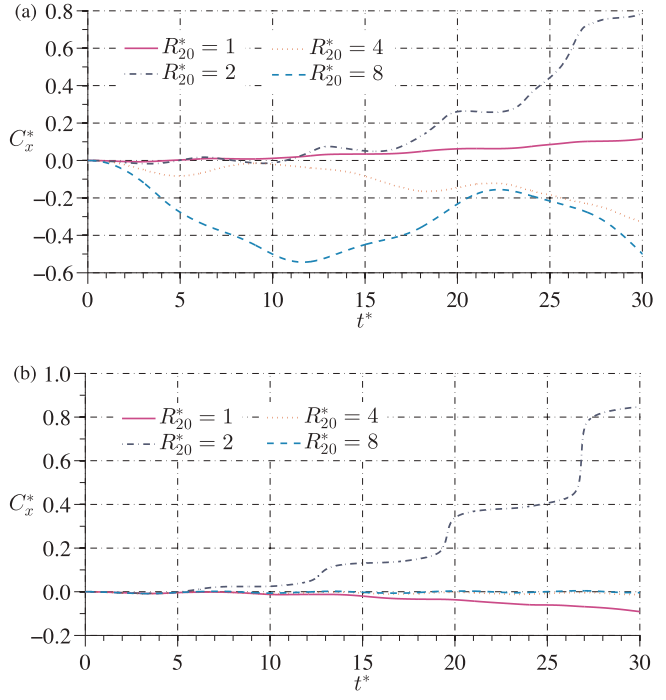

Fig. 15. Time histories of the centroids C_x^* for (a) bubble 1 and (b) bubble 2 for $R_{02}^* = 1,2,4,8$. The remaining parameters are the same as in Fig. 14.

a) When the wave pressure amplitude $p_a > 1$ atm, both bubbles become non-spherical during first few cycles of oscillation, forming two counter jets, generated by high pressure zones behind the jets. The bubble hit by the wave front earlier has a shorter oscillation cycle and a relative lower speed liquid jet. The field pressure can be one order of magnitude larger than the wave pressure amplitude p_a. The bubble behaviour is dominant by the secondary Bjerknes between the two bubbles.
b) When the wave pressure amplitude $p_a < 0.5$ atm, bubble translation is the main characteristic behaviour. Two equal sized bubbles are attracted to each other due to the secondary Bjerknes force. For two unequal sized bubbles, the small bubble leaves away from the large one and the large one does not translate significantly. When the resonance happens, the primary Bjerknes force may lead to the obvious translation of a TMS along the wave direction. However, the separation distance between the bubbles is periodic stable.
c) However, for a TMS under moderate wave amplitude, bubbles undergo both non-spherical oscillation and translation.

Acknowledgements

Xiao Huang thanks FAPERJ — the State of Rio de Janeiro Research Foundation, Brazil for financial support, and Dr. Shuai Li from Harbin Engineering University for the inspiring discussions. A-Man Zhang thanks the National Natural Science Foundation of China (Grant No. 11672081) for financial support. Jian Su thanks CNPq and FAPERJ, Brazil, for financial support.

References

[1] R.E.A. Arndt, Recent advances in cavitation research, Adv. Hydrosci. 12 (1981) 1–78.
[2] R.E.A. Arndt, Cavitation in fluid machinery and hydraulic structures, Annu. Rev. Fluid. Mech. 13 (1) (1981) 273–326.
[3] G.L. Chahine, A. Kapahi, J.K. Choi, C.T. Hsiao, Modeling of surface cleaning by cavitation bubble dynamics and collapse, Ultrason. Sonochem. 29 (2016) 528–549.
[4] N. Ochiai, J. Ishimoto, Computational study of the dynamics of two interacting bubbles in a megasonic field, Ultrason. Sonochem. 26 (2015) 351–360.
[5] A. Skolarikos, G. Alivizatos, J. de la Rosette, Extracorporeal shock wave lithotripsy 25 years later: complications and their prevention, Eur. Urol. 50 (5) (2006) 981–990.
[6] S. Seemann, P. Hauff, M. Schultze-Mosgau, C. Lehmann, R. Reszka, Pharmaceutical evaluation of gas-filled microparticles as gene delivery system, Pharmaceut. Res. 19 (3) (2002) 250–257.
[7] L.A. Crum, Bjerknes forces on bubbles in a stationary sound field, J. Acoust. Soc. Am. 57 (6) (1975) 1363–1370.
[8] T. Barbat, N. Ashgriz, C.-S. Liu, Dynamics of two interacting bubbles in an acoustic field, J. Fluid. Mech. 389 (1999) 137–168.
[9] A. Harkin, T.J. Kaper, A.L.I. Nadim, Coupled pulsation and translation of two gas bubbles in a liquid, J. Fluid. Mech. 445 (2001) 377–411.
[10] N.A. Pelekasis, A. Gaki, A. Doinikov, J.A. Tsamopoulos, Secondary bjerknes forces between two bubbles and the phenomenon of acoustic streamers, J. Fluid. Mech. 500 (2004) 313–347.
[11] Y.N. Zhang, Y.N. Zhang, S.C. Li, The secondary bjerknes force between two gas bubbles under dual-frequency acoustic excitation, Ultrason. Sonochem. 29 (2016) 129–145.
[12] F. Hamaguchi, K. Ando, Linear oscillation of gas bubbles in a viscoelastic material under ultrasound irradiation, Phys. Fluids 27 (11) (2015) 113103.
[13] A.A. Doinikov, A. Bouakaz, Microstreaming generated by two acoustically induced gas bubbles, J. Fluid. Mech. 796 (2016) 318–339.
[14] Y.Q. Liu, Q.X. Wang, Stability and natural frequency of nonspherical mode of an encapsulated microbubble in a viscous liquid, Phys. Fluids 28 (6) (2016) 062102.
[15] S. Nagrath, K.E. Jansen, R.T. Lahey Jr, Computation of incompressible bubble dynamics with a stabilized finite element level set method, Comput. Method. Appl. M 194 (42–44) (2005) 4565–4587.
[16] A.M. Zhang, P.N. Sun, F.R. Ming, An sph modeling of bubble rising and coalescing in three dimensions, Comput. Method. Appl. M 294 (2015) 189–209.
[17] A. Tiwari, C. Pantano, J. Freund, Growth-and-collapse dynamics of small bubble clusters near a wall, J. Fluid. Mech. 775 (2015) 1–23.
[18] R. Han, A.M. Zhang, Y.L. Liu, Numerical investigation on the dynamics of two bubbles, Ocean. Eng. 110 (Part A) (2015) 325–338.
[19] R. Han, S. Li, A.M. Zhang, Q.X. Wang, Modelling for three dimensional coalescence of two bubbles, Phys. Fluids 28 (6) (2016) 062104.
[20] T.T. Bui, E.T. Ong, B.C. Khoo, E. Klaseboer, K.C. Hung, A fast algorithm for modeling multiple bubbles dynamics, J. Comput. Phys. 216 (2) (2006) 430–453.
[21] Z.W. Fu, V. Popov, The aca-bem approach with a binary-key mosaic partitioning for modelling multiple bubble dynamics, Eng. Anal. Bound. Elem. 50 (2015) 169–179.
[22] X. Huang, A.M. Zhang, Y.L. Liu, Investigation on the dynamics of air-gun array bubbles based on the dual fast multipole boundary element method, Ocean. Eng. 124 (2016) 157–167.
[23] N. Bremond, M. Arora, S.M. Dammer, D. Lohse, Interaction of cavitation bubbles on a wall, Phys. Fluids 18 (12) (2006) 121505.
[24] N. Bremond, M. Arora, C.D. Ohl, D. Lohse, Controlled multibubble surface cavitation, Phys. Rev. Lett. 96 (22) (2006) 224501.
[25] Q.X. Wang, K. Manmi, Three dimensional microbubble dynamics near a wall subject to high intensity ultrasound, Phys. Fluids 26 (3) (2014) 032104.

[26] K. Manmi, Q.X. Wang, Acoustic microbubble dynamics with viscous effects, Ultrason. Sonochem. 36 (2017) 427–436.
[27] E. Klaseboer, S.W. Fong, C.K. Turangan, B.C. Khoo, A.J. Szeri, M.L. Calvisi, G.N. Sankin, P.E.I. Zhong, Interaction of lithotripter shockwaves with single inertial cavitation bubbles, J. Fluid. Mech. 593 (2007) 33–56.
[28] M.L. Calvisi, O. Lindau, J.R. Blake, A.J. Szeri, Shape stability and violent collapse of microbubbles in acoustic traveling waves, Phys. Fluids 19 (4) (2007) 047101.
[29] Q.X. Wang, K. Manmi, M.L. Calvisi, Numerical modeling of the 3d dynamics of ultrasound contrast agent microbubbles using the boundary integral method, Phys. Fluids 27 (2) (2015) 022104.
[30] Q.X. Wang, J.R. Blake, Non-spherical bubble dynamics in a compressible liquid. Part 1. Travelling acoustic wave, J. Fluid. Mech. 659 (2010) 191–224.
[31] Q.X. Wang, J.R. Blake, Non-spherical bubble dynamics in a compressible liquid. Part 2. Acoustic standing wave, J. Fluid. Mech. 679 (2011) 559–581.
[32] Q.X. Wang, The evolution of a gas bubble near an inclined wall, Theor. Comp. Fluid. Dyn. 12 (1) (1998) 29–51.
[33] A.M. Zhang, Y.L. Liu, Improved three-dimensional bubble dynamics model based on boundary element method, J. Comput. Phys. 294 (2015) 208–223.
[34] K. Tanizawa, A nonlinear simulation method of 3-d body motions in waves (1st report) formulation of the method with acceleration potential, J. Soc. Nav. Arch. Jpn. 1995 (178) (1995) 179–191.
[35] G.X. Wu, Hydrodynamic force on a rigid body during impact with liquid, J. Fluid. Struct. 12 (5) (1998) 549–559.
[36] H. Wadell, Volume, shape, and roundness of quartz particles, J. Geol. 43 (3) (1935) 250–280.
[37] C.-D. Ohl, M. Arora, R. Dijkink, V. Janve, D. Lohse, Surface cleaning from laser-induced cavitation bubbles, Appl. Phys. Lett. 89 (7) (2006) 074102.
[38] C.C. Coussios, R.A. Roy, Applications of acoustics and cavitation to noninvasive therapy and drug delivery, Annu. Rev. Fluid. Mech. 40 (1) (2008) 395–420.
[39] K.S. Suslick, Sonochemistry, Science 247 (4949) (1990) 1439–1445.
[40] M.L. Calvisi, J.I. Iloreta, A.J. Szeri, Dynamics of bubbles near a rigid surface subjected to a lithotripter shock wave. Part 2. Reflected shock intensifies non-spherical cavitation collapse, J. Fluid. Mech. 616 (2008) 63–97.
[41] T.G. Leighton, A.J. Walton, M.J.W. Pickworth, Primary bjerknes forces, Eur. J. Phys. 11 (1) (1990) 47.